



AMERICAN METEOROLOGICAL SOCIETY

Journal of Climate

EARLY ONLINE RELEASE

This is a preliminary PDF of the author-produced manuscript that has been peer-reviewed and accepted for publication. Since it is being posted so soon after acceptance, it has not yet been copyedited, formatted, or processed by AMS Publications. This preliminary version of the manuscript may be downloaded, distributed, and cited, but please be aware that there will be visual differences and possibly some content differences between this version and the final published version.

The DOI for this manuscript is doi: 10.1175/JCLI-D-16-0367.1

The final published version of this manuscript will replace the preliminary version at the above DOI once it is available.

If you would like to cite this EOR in a separate work, please use the following full citation:

Zhu, J., W. Wang, and A. Kumar, 2016: Simulations of MJO Propagation across the Maritime Continent: Impacts of SST Feedback. *J. Climate*. doi:10.1175/JCLI-D-16-0367.1, in press.

© 2016 American Meteorological Society



1

2 **Simulations of MJO Propagation across the Maritime Continent:**

3 **Impacts of SST Feedback**

4

5

6 Jieshun Zhu^{1,2*}, Wanqiu Wang¹ and Arun Kumar¹

7

8

9

10

11 ¹Climate Prediction Center,
12 NOAA/NWS/NCEP, College Park, Maryland, USA

13

14

15

16 ²Earth System Science Interdisciplinary Center, University of Maryland, College Park,
17 Maryland, USA

18

19

20

21

22

23 *Corresponding author's address:*

24 Dr. Jieshun Zhu

25 Climate Prediction Center,

26 5830 University Research Court, College Park, MD 20740.

27 E-mail: jieshun.zhu@noaa.gov

28 **Abstract**

29 The observed Madden-Julian oscillation (MJO) tends to propagate eastward across the
30 Maritime Continent from the eastern equatorial Indian Ocean to the western Pacific. However,
31 numerical simulations present different levels of fidelity in representing the propagation,
32 especially for the tropical convection associated with the MJO. This study conducts a series of
33 coupled simulations using the NCEP CFSv2 to explore the impacts of SST feedback and
34 convection parameterization on the propagation simulations.

35 Firstly, two simulations differing in the model horizontal resolutions are conducted. The
36 MJO propagation in these two simulations is found generally insensitive to the resolution
37 change. Further, based on the CFSv2 with a lower resolution, two additional experiments are
38 performed with model SSTs nudged to climatologies with different time scales representing
39 different air-sea coupling strength. It is demonstrated that weakening the air-sea coupling
40 strength significantly degrades the MJO propagation simulation, suggesting the critical role of
41 SST feedback in maintaining MJO propagation.

42 Lastly, the sensitivity to convection parameterization is explored by comparing two
43 simulations with different convection parameterization schemes. Analyses of these simulations
44 indicate that including air-sea coupling alone in a dynamical model does not result in realistic
45 maintenance of the MJO eastward propagation without the development of favorable SST
46 conditions in the western Pacific. In both observations and one simulation with realistic MJO
47 propagations, the pre-conditioning of SSTs are strongly affected by surface latent heat fluxes that
48 are modulated by surface wind anomalies in both zonal and meridional directions. The
49 diagnostics highlight the critical contribution from meridional winds in wind speed variations,
50 which has been neglected in most MJO studies.

51 **1. Introduction**

52 The Madden-Julian oscillation (MJO) is the primary mode of tropical intraseasonal
53 climate variability in the boreal winter and spring (Madden and Julian 1971; Zhang 2005). It
54 manifests as a planetary-scale system with organized multi-scale convection and large-scale
55 circulation, and is featured by its eastward propagation along the equator. During a typical MJO
56 event, a positive convection/rainfall anomaly develops over the western Indian Ocean, while
57 convection tends to be suppressed further east over the western Pacific. Over the course of the
58 following 30–60 days, the enhanced convective anomaly in the Indian Ocean intensifies and
59 propagates across the Maritime Continent and the western-central Pacific Ocean.

60 The simulation of the MJO has become a benchmark test for the performance of climate
61 models in the tropics. Although many general circulation models (GCMs) have improved
62 representations of the MJO, many shortcomings still remain, for example, in the simulation of
63 the period, amplitude, seasonality, and geographical dependence of the MJO (Slingo et al. 1996;
64 Lin et al. 2006; Hung et al., 2013; Jiang et al., 2015). A common shortcoming in many GCMs is
65 that the eastward propagation of convection from the Indian Ocean into the west Pacific (i.e., the
66 propagation across the Maritime Continent) remains often poorly represented with standing
67 oscillations of convective activity over the Indian Ocean or west Pacific (Jiang et al. 2015). The
68 model bias in the propagation of MJO across the Maritime Continent has been one of
69 motivations for the "Year of the Maritime Continent (YMC)"
70 (<http://www.bmkg.go.id/ymc/default.bmkg>), an international project with an overarching goal of
71 "observing the weather-climate system of the Earth's largest archipelago to improve
72 understanding and prediction of its local variability and global impact."

73 Simulations of the MJO have been found sensitive to model configurations. Among
74 various factors, convection parameterization is considered as the foremost one (Zhang et al.
75 2006). Studies have suggested that the simulated MJO strongly depends on the criteria for the
76 onset of the convection, e.g., the convection entrainment rate and critical relative humidity
77 (Tokioka et al. 1988; Wang and Schlesinger 1999; Zhang and Mu 2005; Bechtold et al. 2008;
78 Lin et al. 2008). Meanwhile, application of different convection schemes may also result in
79 different levels of fidelity in representing the MJO. For example, based on the NCEP Climate
80 Forecast System, version 1 (CFSv1), Seo and Wang (2010) performed a series of experiments to
81 explore the impacts of various factors on the simulation of the MJO. They found that the
82 simulation strongly depended on the convection parameterization, and the use of the Relaxed
83 Arakawa-Schubert (RAS) cumulus parameterization of Moorthi and Suarez (1999) produced a
84 significantly better representation of the MJO with more realistic periodicity, spectral power, and
85 eastward propagation than simplified Arakawa-Schubert (SAS) cumulus parameterization (Pan
86 and Wu 1995). The superiority of RAS over SAS in the MJO simulations was also achieved by
87 Wang et al. (2015) using the atmospheric component of CFSv2 (Saha et al. 2014). Meanwhile,
88 Bechtold et al. (2008) also showed that improvements to convection and diffusion were
89 responsible for an improved representation of the MJO in the ECMWF Integrated Forecast
90 System.

91 Another process that affects the MJO is the representation of air–sea interaction.
92 Observational diagnoses have shown coherent variations in surface heat fluxes, SST and
93 convection associated with the MJO (e.g., Krishnamurti et al. 1988; Shinoda et al. 1998;
94 Woolnough et al. 2000; Kumar et al. 2013). Many numerical studies also noted improved MJO
95 simulations when an atmosphere-only GCM (AGCM) is coupled to an ocean model (e.g., Flatau

96 et al. 1997; Waliser et al. 1999; Kemball-Cook et al. 2002; Inness et al. 2003; Zhang et al. 2006),
97 confirming the role of ocean feedbacks in the MJO life cycle. Moreover, studies also found that
98 the inclusion of air–sea coupling could extend the MJO predictability and enhance prediction
99 skill of the tropical intraseasonal oscillation (e.g., Vitart et al. 2007; Fu et al. 2008; Pegion and
100 Kirtman 2008; Shelly et al. 2014). Prominent ocean-atmosphere coupled processes are also
101 simulated during the propagation of MJO events with high prediction skill in the ECMWF
102 ensemble prediction system (Kim et al. 2016).

103 The role of SST feedback is also highlighted in many MJO theories, e.g., the air-sea
104 convective interaction (ASCII) mechanism that was proposed by Flatau et al. (1997) based on
105 observational analysis and examined by their simplified experiments. The ASCII mechanism
106 relies on the climatological low-level westerly wind in the region through which the convection
107 propagates. Particularly, the zonal wind anomalies associated with the inflow into the convective
108 region strengthen or weaken the surface wind, which reduce or enhance the latent heat flux
109 (LHF) at the ocean surface. Further, variations in solar shortwave flux (SWF) at the surface
110 associated with MJO-related changes in cloudiness also occur. The combination of these flux
111 variations can induce SST anomalies to the east and west of the convective region. The zonal
112 SST gradient causes zonal changes in surface moist static energy and provides surface forcing,
113 which induces the convection to move toward the east.

114 Coupling an AGCM to an interactive ocean model, however, is not a panacea for
115 problems of simulating the MJO in an uncoupled GCM (Hendon 2000). In fact, many coupled
116 atmosphere–ocean models still exhibit systematic errors in both MJO simulations (Lin et al.
117 2006; Hung et al. 2013; Jiang et al., 2015) and predictions (Wang et al. 2014). There are
118 investigations suggesting that other aspects of the GCM configuration, such as the treatment of

119 cumulus convection and model resolution, could also affect the response of the MJO to air-sea
120 interactions (e.g., Seo and Wang 2010; Crueger et al. 2013). For example, Crueger et al. (2013),
121 based on ECHAM6, found that the effect of air-sea coupling on the MJO propagation
122 simulations is more evident at high resolution. Furthermore, only a small sub-set of experiments
123 demonstrated that coupling could even degrade the representation of the MJO in coupled climate
124 simulations (Hendon 2000; Liess et al. 2004). Studies are also devoted to understand reasons for
125 degradation in MJO simulation, and it has been mostly linked to biases in the CGCM mean state
126 (e.g., Hendon 2000; Liess et al. 2004; Zhang 2005). For instance, Hendon (2000) attributed the
127 degradation to errors in the basic state climatology of the model (particularly the lack of mean
128 surface westerlies across much the warm pool) and too weak latent heat flux anomalies.

129 Inness and Slingo (2003), based on the third Hadley Centre Coupled Ocean-Atmosphere
130 General Circulation Model (HadCM3), found that, while coupling improved the eastward
131 propagation of convection across the Indian Ocean, it could not make it propagate further
132 eastwards and into the west Pacific. Inness et al. (2003) further demonstrated that it was also
133 errors in the low-level zonal wind component in the west Pacific that prevented the MJO from
134 propagating into the region, a result which was confirmed by their flux-corrected simulations.
135 The two model studies are generally consistent with the ASCII mechanism (Flatau et al. 1997),
136 and they all emphasize the critical role of the low-level zonal winds. On the other hand, in Seo
137 and Wang (2010), the problem of simulating the MJO in CFSv1 with the SAS convection
138 scheme was attributed to the too low fraction of the stratiform rainfall relative to the total rainfall
139 over the MJO development region.

140 In general, the effect of air-sea coupling on the MJO simulations could be model-
141 dependent, so is the physical reasoning behind. Thus, assessment of various factors influencing

142 MJO simulations is required across diverse models. However, as recognized by Demott et al.
143 (2015), in such studies the primary attention has been paid to inter-GCM variations in the effects
144 of coupling than to intra-GCM variations related to the model's physical parameterizations and
145 configurations. The purpose of this study is to contribute to the continuing efforts towards
146 understanding problems on the MJO simulations. For this purpose, a series of coupled
147 simulations are conducted based on a single GCM, i.e., the NCEP CFSv2 (Saha et al. 2014).
148 These experiments differ in their model configurations, including horizontal resolutions,
149 convection parameterizations and the strength of SST feedback.

150 Our focus is on the simulations of MJO propagation across the Maritime Continent. The
151 Maritime Continent has been known as an MJO “propagation barrier” for many GCMs, but its
152 role in supporting or hindering the MJO has not been well understood (Inness and Slingo 2006).
153 By diagnosing the experiments, we address the following two questions: (i) Is the air-sea
154 interaction (or SST feedback) critical for simulating the eastward propagation of the MJO, and if
155 yes, (ii) what processes are responsible for the development of SST conditions favorable for the
156 MJO propagation across the Maritime Continent. Question (i) is explored by comparing
157 simulations with predicted SSTs nudged to climatological values with different strengths
158 representing different degree of air-sea coupling. For Question (ii), we investigate physical
159 processes contributing to SST evolutions in observations and two CFSv2 simulations with
160 contrasting levels of fidelity in simulating the MJO eastward propagation, which results from
161 different convection schemes.

162 The paper is organized as follows. The model, the experimental design, and the datasets
163 are described in the next section. The results are presented in section 3, where factors influencing

164 MJO propagation simulations are explored with a focus on the SST feedback. The summary and
165 discussion are given in section 4.

166

167 **2. Models, Experiments and Datasets**

168 *2.1 Models*

169 In this study, the NCEP CFSv2 (Saha et al. 2014) is used for a series of MJO simulation
170 experiments. In addition, CFSv2 with a lower resolution (referred to as CFSv2L) is also applied
171 for experiments. The ocean component (the GFDL MOM version 4) of CFSv2 (CFSv2L) is
172 configured for the global ocean with a horizontal grid of $0.5^\circ \times 0.5^\circ$ ($1^\circ \times 1^\circ$) poleward of 30°S and
173 30°N and meridional resolution increasing gradually to 0.25° (0.33°) between 10°S and 10°N .
174 The vertical coordinate is geopotential (z -) with 40 levels (27 of them in the upper 400 m), with
175 maximum depth of approximately 4.5 km. The atmospheric component of CFSv2 (CFSv2L) has
176 horizontal resolutions at T126 (T62) with 64 vertical levels in a hybrid sigma-pressure
177 coordinate. The two components exchange surface momentum, heat and freshwater fluxes, as
178 well as SSTs, every 30 (60) minutes in CFSv2 (CFSv2L).

179 Different from the standard configuration of CFSv2 (Saha et al. 2014) which uses the
180 2007 version of the NCEP operational global forecast system (GFS), the atmospheric component
181 in the two coupled systems used in this study (CFSv2 and CFSv2L) is the 2011 version of the
182 NCEP GFS, but the model physics are configured as in Saha et al. (2014). In this study, the
183 following two of the convection schemes built in the model are used for experiments.

184 1) The Simplified Arakawa–Schubert (SAS) cumulus convection scheme (Pan and Wu 1995),
185 which was used in Saha et al. (2014). The SAS scheme is based on the Arakawa and
186 Schubert one (Arakawa and Shubert 1974), and simplified by Grell (1993) to consider only

187 one cloud instead of a spectrum of clouds. Convection occurs when the cloud work function
188 exceeds a certain threshold. A simple trigger is employed, which requires that the level of
189 free convection must exist and must be within the distance of 150 hPa of the parcel starting
190 level.

191 2) The Relaxed Arakawa–Schubert (RAS) cumulus convection scheme, which in GFS was
192 developed by Moorthi and Suarez (1992, 1999). The RAS scheme simplifies the entrainment
193 relation, and assumes that the normalized mass flux is a linear function of height rather than
194 being exponential as in the original Arakawa and Shubert scheme. In addition, rather than
195 requiring that “quasi equilibrium” of the cloud ensemble be achieved each time, the scheme
196 only relaxes the ambient atmospheric state toward equilibrium.

197

198 *2.2 Experiments*

199 Based on the two coupled systems (CFSv2 and CFSv2L) with different horizontal
200 resolutions, five simulation experiments are conducted (Table 1). All the five simulations are
201 initialized from the Climate Forecast System Reanalysis (CFSR; Saha et al. 2010) state on 1
202 January 1980, and run for 25 years. All model diagnoses are based on outputs of last 20 years.

203 • The first two simulations are based on CFSv2 and CFSv2L, both using the RAS convection
204 scheme (referred to as CFSv2_RAS and CFSv2L_RAS; Table 1). The comparison between
205 CFSv2_RAS and CFSv2L_RAS explores the impact of model resolutions on MJO
206 simulations.

207 • The third and fourth experiments (referred to as CFSv2L_RAS_SST10dy and
208 CFSv2L_RAS_SST1dy; Table 1) are designed to explore the role of SST feedback by
209 comparing them with CFSv2L_RAS. In the two experiments, all settings are the same as

210 CFSv2L_RAS, except that predicted SSTs during integrations are nudged to CFSv2L_RAS
211 climatological SSTs with seasonal cycle. Nudging to the CFSv2L_RAS SSTs other than the
212 observational counterpart has the advantage of removing the possible influence of differences
213 in the basic state climate associated with coupled model SST biases. The restoring time
214 scales are chosen as 10 days and 1 day for CFSv2L_RAS_SST10dy and
215 CFSv2L_RAS_SST1dy, respectively. The choice of the 10-day time scale for
216 CFSv2L_RAS_SST10dy takes into account the fact that in observations and CGCMs there
217 are coherent relationships between MJO convections, surface fluxes and SSTs with a lag of
218 around 10 days (e.g., Woolnough et al. 2000; Kumar et al. 2013; DeMott et al. 2015). The
219 use of 1-day time scale for CFSv2L_RAS_SST1dy is to compare the impact when the air-sea
220 interaction is essentially removed.

- 221 • The fifth simulation is based on CFSv2 and the SAS convection scheme (referred to as
222 CFSv2_SAS; Table 1). CFSv2_SAS corresponds to the standard version of CFSv2 (Saha et
223 al. 2014). Its comparison with CFSv2_RAS examines the effect of convection schemes on
224 MJO simulations.

225

226 *2.3 Analysis method and observations*

227 Anomalies are calculated as departures from seasonal climatology which is defined as
228 annual mean plus the first four harmonics of long-term average. To focus on the intraseasonal
229 variability, most analyses are based on intraseasonal anomalies obtained by applying 20~100-day
230 band-pass filtering to the raw daily-mean anomalies. When evaluating the zonal propagation
231 features of the simulated MJO, lead-lag correlations or regressions are calculated for the 10°S–
232 10°N averaged intraseasonal anomalies with respect to the Indian Ocean precipitation (70-100°E,

233 10°S-10°N). To identify the physical factor modulating LHF variations, a simplified bulk
234 formula [i.e., Eq (1)] is used to diagnose LHF based on SST, 2-m specific humidity, 10-m
235 velocity and sea level pressure. In this study, we take surface flux anomalies as being positive
236 *into* the ocean surface. Thus, a positive LHF anomaly corresponds to a *reduction* in evaporation
237 from the ocean.

238 The observational data used for validations include daily SST analyses from the National
239 Centers for Environmental Information (NCEI) using the optimum interpolation (IO) scheme
240 (Reynolds et al. 2007), rainfall estimate from the CPC morphing technique (CMORPH) satellite
241 retrieval (Joyce et al. 2004), and 850-hPa zonal winds (U850), surface shortwave (SWF) and
242 latent heat fluxes (LHF) from the CFSR (Saha et al. 2010). For the LHF calculation based on the
243 simplified bulk formula [i.e., Eq (1)], daily SST, 2-m specific humidity, 10-m velocity and sea
244 level pressure from CFSR are used as well. All the observational diagnoses are based on data
245 during 1998-2014.

246

247 **3. Results**

248 *3.1 The impact of horizontal resolutions on the MJO simulations*

249 The effect of model resolution on the MJO is explored by comparing CFSv2_RAS with
250 CFSv2L_RAS. Investigations about the climatological mean states between these two
251 simulations suggest that the mean biases in SST, the low-level zonal wind and precipitation are
252 generally similar over the tropical Indian Ocean and the western Pacific (figures not shown).

253 For the simulation of the MJO, CFSv2_RAS and CFSv2L_RAS also exhibit the
254 comparable level of fidelity. In terms of spatial distribution of intraseasonal variance (figures not
255 shown), CFSv2_RAS captures some finer structures than CFSv2L_RAS over the Maritime

256 Continent with complex topography, but they are not significantly different on a larger spatial
257 scale. In particular, both models simulate similar and generally realistic variance maps for 850-
258 hPa zonal wind and precipitation featured by large variance over the Indian Ocean and the
259 western Pacific and low variance over the Maritime Continent.

260 The eastward propagation of the MJO is also simulated at the similar level of fidelity.
261 Figs. 1a and 1d shows time-longitude diagrams of intraseasonal precipitation anomalies (colors)
262 and 850-hPa zonal wind anomalies (contours) regressed against the precipitation over the Indian
263 Ocean (70-100°E, 10°S-10°N) for boreal winter. Similar to their observational counterpart (Fig.
264 1c), the simulated MJOs propagates eastward across the Eastern Hemisphere at a speed of
265 around 4m/s, with the westerly wind anomalies lagging behind positive precipitation anomalies
266 by about 5-7 days. In addition, while the precipitation anomalies are generally confined to the
267 Eastern Hemisphere (colors in Figs. 1a, c, d), the 850-hPa zonal wind anomalies could propagate
268 further eastwards in the Western Hemisphere at a faster speed (contours in Figs. 1a, c, d). It is
269 worthy of highlighting that in contrast to most state-of-the-art models that suffer from the MJO
270 “propagation barrier” over the Maritime Continent (Jiang et al. 2015), the MJO in CFSv2_RAS
271 and CFSv2L_RAS is able to propagate across the Maritime Continent as in observations.
272 Comparing CFSv2_RAS with CFSv2L_RAS, a discontinuity in convection is more evident at
273 the Maritime Continent in CFSv2_RAS, which might be due to finer orography (Inness and
274 Slingo 2006) or better resolved surface boundary conditions including land fraction, soil and
275 vegetation parameters (Schiemann et al. 2014) at the higher resolutions in CFSv2_RAS.

276 Accompanying the propagation signal in precipitation anomalies and 850-hPa zonal wind
277 anomalies, intraseasonal anomalies of SST and surface fluxes in observations also exhibit
278 evident eastward propagation (Figs. 2c-5c), which are captured by CFSv2_RAS (Figs. 2a-5a)

279 and CFSv2L_RAS (Figs. 2d-5d) generally well. The lag-longitude diagrams with SST (contours
280 in Figs. 2a, c, d) show warm SST anomalies in the Indian Ocean prior to the convection, and cold
281 SST anomalies after the convection. Associated with the convection in the Indian Ocean, warm
282 SST anomalies appear in the western Pacific. According to the ASCII mechanism (Flatau et al.
283 1997), the zonal SST gradient could induce the convection to move eastwards. The intraseasonal
284 SST anomalies are a response to the air-sea heat flux forcing, as evidenced by a general one
285 quadrant-lag relationship between them (Figures not shown). Further diagnoses suggest that the
286 surface heat flux anomalies are mainly composed of SWF (contours in Figs. 3a, c, d) and LHF
287 (contours in Figs. 4a, c, d). The SWF variations are related to changes in cloudiness associated
288 with the MJO. The LHF variations are mainly modulated by changes in wind speeds with
289 contributions from the zonal wind anomalies as noted in many MJO studies (e.g., Flatau et al.
290 1997; Woolnough et al. 2000; Hendon 2000; Inness et al. 2003). As to be discussed later in
291 Section 3.3, our analysis shows that meridional wind anomalies also have significant
292 contributions to the LHF variations.

293 In summary, the MJO, in terms of its propagation, amplitude and periodicity, in general,
294 is realistically simulated by CFSv2 with the RAS convection. The model horizontal resolution
295 change from T126 to T62 in atmosphere and $0.5^\circ \times 0.5^\circ$ to $1^\circ \times 1^\circ$ in ocean is found to exert
296 negligible effects on the representation of the MJO, particularly in regard to its eastward
297 propagation. The MJO-related relationships between convection, surface fluxes and SST are
298 overall consistent with previous observational diagnoses (e.g., Krishnamurti et al. 1988; Shinoda
299 et al. 1998; Woolnough et al. 2000), and generally follow the ASCII mechanism for the
300 intraseasonal oscillation proposed by Flatau et al. (1997).

301

302 3.2 The role of SST feedback in simulating MJO propagation

303 Considering the comparable level of fidelity in simulating the MJO by CFSv2L_RAS and
304 CFSv2_RAS as demonstrated above, and for faster turnover, CFSv2L_RAS is used for further
305 experiments to explore the role of SST feedback in simulating the MJO propagation. In
306 particular, two experiments (i.e., CFSv2L_RAS_SST1dy and CFSv2L_RAS_SST10dy; Table 1)
307 are done with model SSTs nudged to the CFSv2L_RAS climatological state. The rationale
308 behind the SST nudged experiments is as follows. If the MJO is purely a result of internal
309 atmospheric dynamics, the two nudged experiments should capture similar MJO features as the
310 free run (i.e., CFSv2L_RAS). On the contrary, if substantial differences exist, it will indicate that
311 SST feedback plays a role.

312 The diagnoses of the mean states suggest that the mean biases in SST, the low-level
313 zonal wind and precipitation are almost the same in two SST nudged simulations and
314 CFSv2L_RAS (figures not shown), which is to be expected from the experimental design.
315 However, weakening the air-sea coupling strength has a clear reduction in the intraseasonal
316 variance of 850-hPa zonal wind and precipitation over both the Indian Ocean and the western
317 Pacific (figures not shown); a hint suggesting that SST feedback might be important in the MJO
318 evolution. Also, the variance decrease is more significant in the western Pacific than in the
319 Indian Ocean, suggesting that air-sea coupling might be more important for sustaining the MJO
320 amplitude over the western Pacific.

321 Regarding the simulation of MJO propagation, SST feedback is found to play a critical
322 role. For LHF, its variations over the Indian Ocean and the western Pacific exhibits many similar
323 features in CFSv2L_RAS_SST1dy (contours in Fig. 4e) and CFSv2L_RAS_SST10dy (contours
324 in Fig. 4f) as in CFSv2L_RAS (contours in Fig. 4d). For example, coincident with the

325 precipitation over the Indian Ocean, there are positive LHF anomalies to the east of the
326 precipitation center, which are thought to be important for warm SST there and induce the
327 convection to move eastwards (Flatau et al. 1997). The similarity is because the MJO-related
328 LHF variations are dominated by the wind speed variations (detailed analyses to be presented in
329 Section 3.3), and the winds mainly change as a Gill-type response to the heating in the Indian
330 Ocean.

331 For SWF (contours in Figs. 3d-f), its variations again highly resemble their respective
332 patterns in precipitation (colors in Figs. 2d-f), because of the associated changes in cloudiness. In
333 particular, for both precipitation and SWF anomalies, while they exhibit well-defined eastward
334 propagation in CFSv2L_RAS (Figs. 2d and 3d) as in reality (colors in Fig. 2c and contours in
335 Fig. 3c), such propagation seems absent as the nudging strength is as large as $O(1 \text{ day})^{-1}$ (colors
336 in Fig. 2f and contours in Fig. 3f); instead, a standing component is more evident. Furthermore,
337 while precipitation and SWF anomalies could penetrate through the dateline in CFSv2L_RAS
338 (Figs. 2d and 3d) as in observations (Figs. 2c and 3c), they are generally confined to the west of
339 the western Pacific in CFSv2L_RAS_SST1dy (Figs. 2f and 3f). The feature is consistent with the
340 intraseasonal variance distribution that shows clearly weakened variance over the western Pacific
341 as a result of the strong nudging (figures not shown).

342 The unrealistic intraseasonal features of precipitation (and SWF) simulated by
343 CFSv2L_RAS_SST1dy could be explained by the associated variabilities in SST (contours in
344 Fig. 2f). As a result of strong nudging to the climatological state [i.e., $O(1 \text{ day})^{-1}$], SST exhibits
345 much weaker intraseasonal variations than that in CFSv2L_RAS (Fig. 2d vs. Fig. 2f). Outside the
346 Indian Ocean, there are no clear SST intraseasonal variations in CFSv2L_RAS_SST1dy
347 (contours in Fig. 2f). Without the corresponding warm SST forcing, the overlaying atmosphere

348 will be more stable, hindering convective activity, which is evidenced by low precipitation
349 variations between 140°E and 180°E. Because of the lower variability in precipitation, zonal
350 winds also exhibit lower intraseasonal variations (contours in Fig. 1f). When the nudging
351 strength is weakened to $O(10 \text{ day})^{-1}$ (i.e., CFSv2L_RAS_SST10dy), the SST intraseasonal
352 variations become stronger as expected (contours in Fig. 2e). Consistently, more convection is
353 invoked to the east of 140°E, and precipitations exhibits some level of eastward propagation
354 (colors in Fig. 2e), but the eastward propagation is still weaker than in CFSv2L_RAS (colors in
355 Fig. 2d).

356 Overall, the two SST nudging experiments based on CFSv2L_RAS suggest that SST
357 feedback is critical in maintaining MJO propagation in the model. However, one could ask
358 whether including the SST feedback alone in a coupled atmosphere-ocean model is sufficient for
359 the simulation of the eastward propagation across the Maritime Continent, and if not, what
360 processes are responsible for the unsuccessful simulation. These questions are addressed in next
361 subsection by comparing two coupled simulations with contrasting levels of fidelity in
362 representing the MJO propagation.

363

364 *3.3 The role of convection schemes in the MJO simulations and processes contributing to* 365 *favorable SSTs for MJO propagation*

366 In this part, the sensitivity of MJO simulations to convection schemes is first explored by
367 comparing CFSv2_SAS with CFSv2_RAS. Then, we diagnose physical processes that explain
368 for contrasting levels of fidelity in representing the MJO propagation between them.

369 It should be noted that CFSv2_SAS corresponds to the standard version of CFSv2 (Saha
370 et al. 2014), in which the MJO has been evaluated in terms of simulations and predictions

371 (Weaver et al. 2011; Wang et al. 2014). It has been found that in CFSv2 with the SAS
372 convection scheme (i.e., CFSv2_SAS; Saha et al. 2014), the simulated MJO propagates slower
373 than the observed with difficulties traversing the Maritime Continent into the western Pacific
374 (Weaver et al. 2011). Consistent with experiments based on CFSv1 (Seo and Wang 2010) and
375 the atmospheric component of CFSv2 (Wang et al. 2015), our experiments suggest that the MJO
376 propagation in CFSv2 is clearly better represented by replacing the SAS convection scheme (Pan
377 and Wu 1995) with RAS (Moorthi and Suarez 1992, 1999). In particular, in CFSv2_RAS (Fig.
378 1a), the simulated MJOs propagate realistically eastwards across the Eastern Hemisphere at a
379 speed of around 4m/s, and the zonal wind anomalies lag behind the precipitation anomalies by
380 about 5-7 days, both resembling the observed features (Fig. 1c). In contrast, the intraseasonal
381 precipitation anomalies in CFSv2_SAS clearly stop propagating when encountering the Maritime
382 Continent (colors in Fig. 1b), even though the zonal wind anomalies, as a Gill-type response to
383 heating in the Indian Ocean, propagate further and cross the dateline. The MJO propagation bias
384 is also evident in most coupled models in which SST feedback has been included (e.g., Jiang et
385 al. 2015). Therefore, it can be concluded that the inclusion of SST feedback alone in coupled
386 models is not sufficient for maintaining the MJO eastward propagation across the Maritime
387 Continent.

388 In fact, despite of SST feedback being included in both CFSv2_RAS and CFSv2_SAS,
389 quite different intraseasonal SST anomalies occur between them. In CFSv2_RAS (Fig. 2a),
390 coincident with the precipitation in the Indian Ocean, warm SST anomalies appear in the western
391 Pacific, a feature as in observations (Fig. 2c). According to the ASCII mechanism (Flatau et al.
392 1997), the warm SST anomalies favor the eastward propagation of convection, traversing the
393 Maritime Continent. However, in CFSv2_SAS, intraseasonal SST anomalies are generally

394 confined within the Indian Ocean and well organized warm SST anomalies are absent in the
395 western Pacific (contours in Fig. 2b), resulting in an unfavorable condition in the western Pacific
396 for convection development and thus preventing the eastward propagation from the Indian
397 Ocean.

398 Further diagnoses suggest that, between two important factors (i.e., SWF and LHF) for
399 the intraseasonal SST variations in the western Pacific, LHF is the dominant one for the
400 difference between CFSv2_RAS and CFSv2_SAS. For SWF, in CFSv2_RAS (Fig. 3a),
401 CFSv2_SAS (Fig. 3b) and observations (Fig. 3c), the western Pacific Ocean is all generally
402 forced by positive SWF anomalies at the lag times from -10 days to 0, which could drive warm
403 SST anomalies locally. However, for LHF in the western Pacific ocean, CFSv2_SAS (Fig. 4b) is
404 very different from CFSv2_RAS (Fig. 4a) and observations (Fig. 4c). In CFSv2_RAS and
405 observations, positive LHF anomalies are evident in the western Pacific at the lag times from -10
406 days to 0, which will reinforce the SWF effect on SST, resulting in local warm anomalies (colors
407 in Figs. 4a, c) coincident with precipitation in the Indian Ocean. In contrast, in CFSv2_SAS (Fig.
408 4b), for the same lag times negative LHF anomalies are present, which will offset the SWF effect
409 and favor near-normal SST condition over the region (colors in Fig. 4b). The contrasting LHF
410 difference between CFSv2_SAS and CFSv2_RAS/observations is more evident in Fig. 5, which
411 calculates the lead-lag correlations between the intraseasonal precipitation anomalies over the
412 Indian Ocean and the intraseasonal LHF anomalies over (120-140°E, 10°S-10°N) for boreal
413 winter. It is clear that, over the lag time range from -15 days to 30 days the correlations in
414 CFSv2_RAS is generally in-phase with the observed, but they are almost in an opposite phase
415 with those in CFSv2_SAS (Fig. 5). Particularly, LHF has opposite signs between CFSv2_SAS
416 and CFSv2_RAS/observations at the lag time from -10 days to 0, which accumulatively

417 contributes the SST anomalies at the 0-lag time.

418 To further explore factors influencing the intraseasonal LHF anomalies, we re-calculate
419 LHF based on the bulk formula with associated physical variables. By omitting the parameters
420 that are nearly constant, to the first order LHF is calculated as follows:

$$421 \quad LHF \sim w(q_a - q_s), \quad (1)$$

422 where w is the 10-m wind speed, q_a is the 2-m specific humidity, and q_s is the saturation specific
423 humidity at the ocean surface. By repeating Fig. 5 but using the re-calculated LHF based on Eq.
424 (1), the new lead-lag correlations (figures not shown, but the lead-lag regressions are shown in
425 Fig. 6 as black curves) are found almost identical to those in Fig. 5 for both model simulations
426 and observations, providing a justification to our LHF calculations.

427 According to Eq. (1), the intraseasonal LHF anomalies could be decomposed as follows:

$$428 \quad \delta LHF \sim \delta w(\bar{q}_a - \bar{q}_s) + \bar{w}(\delta q_a - \delta q_s) + \varepsilon, \quad (2)$$

429 where δ means the intraseasonal (20–100-day filtered) component, $\bar{(\cdot)}$ means the climatological
430 mean during November-April, and ε is the residual term (i.e., the nonlinear term which is the
431 product of anomalous wind speeds and anomalous near-surface vertical gradients of moisture).
432 Fig. 6 presents the lead-lag regressions of δLHF , $\delta w(\bar{q}_a - \bar{q}_s)$, $\bar{w}\delta q_a$, $-\bar{w}\delta q_s$ and ε against the
433 intraseasonal precipitation anomalies over the Indian Ocean for boreal winter. It is clear that, in
434 model simulations and observations the nonlinear term (ε) is negligibly small in association
435 with the MJO (dashed curves in Fig. 6). Also, while the regressions with $\bar{w}\delta q_a$ (green curves in
436 Fig. 6) and $-\bar{w}\delta q_s$ (blue curves in Fig. 6) are comparable in magnitude in observations and two
437 model simulations, they are generally in opposite phase and cancel each other at the lag times
438 from -30 days to 30 days. As a result, the combined contributions of $\bar{w}\delta q_a$ and $-\bar{w}\delta q_s$ in δLHF

439 are also generally small. In contrast, for observations and two model simulations, the
440 regressions with the term $\delta w(\bar{q}_a - \bar{q}_s)$ (red curves in Fig. 6) are highly correlated with those
441 about δLHF , which suggests that the intraseasonal LHF anomalies are mostly controlled by
442 the product of anomalous wind speeds and mean near-surface vertical gradients of moisture [i.e.,
443 $\delta w(\bar{q}_a - \bar{q}_s)$].

444 Furthermore, it is encouraging to note that, CFSv2 with the RAS convection not only
445 realistically captures the lead-lag relationship of LHF with the Indian Ocean precipitation, but
446 those about the decomposed terms associated with LHF are also realistically represented. For
447 example, in observations, the product of mean wind speeds and anomalous near-surface vertical
448 gradients of moisture (i.e., $-\bar{w}\delta q_s$; green curve in Fig. 6a) over (120-140°E, 10°S-10°N) is
449 featured by a peak of positive (negative) correlation with the precipitation in the Indian Ocean at
450 the lag time of around 4 days (-12 days), which is also captured by CFSv2_RAS (green curve in
451 Fig. 6b). In fact, this feature also seems to be captured by CFSv2_SAS at a certain level (green
452 curve in Fig. 6c). However, for the most important term for LHF --- $\delta w(\bar{q}_a - \bar{q}_s)$ (red curves in
453 Fig. 6), remarkable difference is evident between CFSv2_SAS and CFSv2_RAS/observations.
454 Particularly, in association with intraseasonal SST anomalies over the western Pacific at the 0-
455 day lag, $\delta w(\bar{q}_a - \bar{q}_s)$ makes a positive contribution in CFSv2_RAS/observations but a negative
456 contribution in CFSv2_SAS, which can be seen from their integrated effects during the lag times
457 from -10 days to 0. Therefore, it is concluded that it is the difference in simulated wind speeds
458 that plays a major role in the difference of intraseasonal LHF variations over the western Pacific,
459 which results in substantial difference in local SST conditions between CFSv2_SAS and
460 CFSv2_RAS.

461 As a further step in diagnostics, we are interested to know the contribution from each of

462 the wind components (i.e., the zonal and meridional winds). In Fig. 7, we calculate the lead-lag
463 regressions of intraseasonal w^2 , u^2 and v^2 anomalies [averaged over (120-140°E, 10°S-10°N)]
464 against the intraseasonal precipitation anomalies over the Indian Ocean for boreal winter, where
465 w^2 is the square of 10-m wind speed, and u^2 (v^2) is the square of 10-m zonal (meridional) wind
466 component. Note that the regressions in Fig.7 have been multiplied with a minus sign to mimic
467 the sign of surface heat flux into the ocean. Comparing CFSv2_RAS (Fig. 7b) and observations
468 (Fig. 7a), the lead-lag regressions are again generally in the same phase for intraseasonal w^2 , u^2
469 and v^2 anomalies.

470 We next focus on the lag times close to 0 when dramatically different SST conditions
471 appear in the western Pacific between CFSv2_SAS and CFSv2_RAS/observations (Fig. 2). In
472 CFSv2_RAS and the observation (Figs. 7a and 7b), the total wind speed (red curves) is
473 weakened for most of the lag time after day -20 and before the zero-day lag, and the change in
474 both the zonal and meridional components contribute to the total wind speed weakening. The
475 regression for $-u^2$ (blue curves) becomes positive after the lag time of day -22 in the observation
476 and day -29 in CFSv2_RAS, increases to a positive maximum value at days -13 to -14, and then
477 decreases and reaches a negative minimum value around day 2. The regression for $-v^2$ increases
478 from zero around day -14 in the observation and day -17 in CFSv2_RAS, reaching a positive
479 maximum value around day -3. The net effect of the two wind components in CFSv2_RAS and
480 observations is a positive regression for $-w^2$, corresponding to weakening of total wind speed,
481 during most of the lag time from day -20 to 0. The weakening of the wind speed is largely from
482 the change in the zonal component before day -9. After day -0, the weakening of the wind speed
483 is dominated by the change in the meridional wind.

484 In contrast, in CFSv2_SAS (Fig. 7c), the wind speed weakens before day -9 after which

485 the wind speed becomes stronger, and the contribution from the meridional component is much
486 smaller compared to that in the observation and CFSv2_RAS. Both u^2 and v^2 in CFSv2_SAS are
487 quite different from those in the CFSv2_RAS and observation. For u^2 (blue curve in Figs. 7c), the
488 negative regression values for $-u^2$ before the zero-day lag starts at day -10 in CFSv2_SAS, much
489 earlier than that in the observation (day -3) and CFSv2_RAS (day -6), and the amplitude of the
490 negative regression values for $-u^2$ in CFSv2_SAS is much larger than in the observation and
491 CFSv2_RAS. For v^2 (green curve in Figs. 7c), the amplitude of the positive regression in
492 CFSv2_SAS is quite small with a local minimum at the lag time around day -3 in contrast to a
493 local maximum in CFSv2_RAS and observations. The weak positive regression for the
494 meridional component and the large negative regression for the zonal component in CFSv2_SAS
495 result in net strengthened wind over (120-140°E, 10°S-10°N) prior to the 0-lag time, which is
496 contrary to the weakened total wind speed due to reduced amplitude of meridional velocity in the
497 CFSv2_RAS and observation. It should be noted that, the difference of the intraseasonal wind
498 anomalies between CFSv2_SAS and CFSv2_RAS cannot be attributed to the difference in
499 climatological state as the climatological surface winds are overall similar between the two
500 simulations (figures not shown).

501 The difference of u^2 and v^2 between two simulations is also evident in Fig. 8, which
502 demonstrates the spatial patterns of above regressions averaged over the lag times from -10 days
503 to 0. East of 120°E, in CFSv2_RAS, similar to observations, $-u^2$ is featured by positive
504 regressions coherent with negative regressions, but that in CFSv2_SAS is clearly dominated by
505 positive regressions. Also, while $-v^2$ shows uniform positive regressions east of 120°E in
506 CFSv2_RAS and observations, for CFAv2_SAS it has clear negative regressions.

507 To summarize, the coupled experiments with different convection schemes indicate that
508 air-sea coupling alone cannot maintain the MJO eastward propagation across the Maritime
509 Continent, but favorable pre-conditioning of SSTs must be realistically developed in models.
510 Further, for the development of such SST conditions, not only the zonal surface winds should be
511 realistically represented as highlighted in previous MJO studies (e.g., Flatau et al. 1997; Hendon
512 2000; Inness and Slingo 2003, Liess et al. 2004; Zhang 2005), but the meridional component is
513 also equally important, a fact that has been ignored in most MJO studies.

514

515 **4. Conclusion and discussion**

516 In this study, we contribute to the continuing efforts in understanding the causes for
517 problems in the MJO simulations, particularly in its eastward propagation. In particular, a series
518 of coupled simulations are conducted based on the NCEP Climate Forecast System, version 2
519 (CFSv2) to explore the sensitivity of the MJO simulations to changes in model configurations,
520 including horizontal resolutions, air-sea coupling and convection schemes. The model results are
521 also compared with observations to verify its fidelity.

522 Firstly, two simulations with different horizontal resolutions are compared, which are
523 based on the RAS convection scheme. It is found that the MJO, in terms of its propagation,
524 amplitude and periodicity, is generally realistically simulated. Furthermore, the model horizontal
525 resolution change from T126 for the atmosphere and $0.5^{\circ} \times 0.5^{\circ}$ for the ocean to T62 for the
526 atmosphere and $1^{\circ} \times 1^{\circ}$ for the ocean exerts negligible influence on the representation of the MJO.
527 In addition, the MJO-related relationships between convection, surface fluxes and SST are
528 overall consistent with previous observational diagnoses (e.g., Krishnamurti et al. 1988; Shinoda

529 et al. 1998; Woolnough et al. 2000), and generally follow the ASCII mechanism for the
530 intraseasonal oscillation proposed by Flatau et al. (1997).

531 Further, based on the CFSv2 with the lower resolution (CFSv2L), two more experiments
532 were performed with model SSTs nudged to model climatologies at the restoring time scales of
533 10 days and 1 day, respectively. It is found that weakening the air-sea coupling strength
534 significantly degraded MJO propagation, suggesting the critical role of SST feedback in
535 maintaining MJO propagation.

536 Lastly, the sensitivity to convection parameterization is explored by comparing two
537 CFSv2 simulations with the RAS and SAS convection parameterization schemes. Analyses
538 indicated that, while CFSv2 with RAS simulates the MJO quite realistically, the MJO-related
539 convection in the simulation with SAS could not propagate eastward across the Maritime
540 Continent. It suggests that air-sea coupling alone cannot maintain the MJO eastward propagation
541 across the Maritime Continent. Further analyses indicated that favorable SST conditions must be
542 realistically developed in models. In both observations and the simulation with RAS, warm SST
543 anomalies corresponding to precipitation in the Indian Ocean were present to the east of the
544 Maritime Continent. This SST signal, however, was absent in the simulation based on SAS. The
545 difference in surface latent heat fluxes was further identified as the major factor resulting in the
546 SST difference.

547 Detailed diagnoses of the latent heat flux suggest that, in both observations and the RAS
548 simulation, east of the Maritime Continent the latent heat flux intraseasonal variability was
549 generally controlled by surface wind speeds. Prior to the local warm SST anomalies, mostly as a
550 result of weakened meridional surface wind, the surface wind becomes weaker than normal,
551 which leads to less latent heat flux out of the ocean, accumulatively responsible for the late warm

552 SST anomalies. On the other hand, as a result of unrealistic representation of both zonal and
553 meridional winds in the SAS simulation, the surface wind became stronger than normal,
554 resulting in more latent heat flux out of the ocean. When working together with the surface solar
555 shortwave flux, near-normal SST condition is forced to the east of the Maritime Continent. As a
556 result, in the SAS simulation the MJO-related convection stopped propagating further eastwards.

557 It is worthy to highlight that, in the development of favorable SST conditions for the
558 MJO propagation, not only the zonal surface winds should be realistically represented as noted in
559 previous MJO studies (e.g., Flatau et al. 1997; Hendon 2000; Inness and Slingo 2003, Liess et al.
560 2004; Zhang 2005), but the meridional component is also equally important. The factor has been
561 largely neglected in most of the previous MJO studies. Further studies are required to understand
562 how the surface winds are affected by the different convection schemes, which represents the
563 next challenge.

564 It is also noted that some studies (e.g., the moisture mode theory) suggested that the
565 horizontal advection of moisture is an important factor for MJO propagation (Kim et al. 2014).
566 Thus, the moisture mode theory is another aspect that may help understand the MJO differences
567 simulated by two convection schemes, but it is not the focus of the paper which focuses on the
568 ocean surface impact. In addition, an analysis about mixed layer depth (MLD; figures not shown)
569 in CFSv2L_RAS indicates that MLD varies nearly in phase with intraseasonal SST variations
570 with shallow MLD accompanying warm SST. Considering that as a response to fixed heat fluxes
571 shallower MLD will result in warmer SST, the warm SST east of 120°E might involve upper
572 ocean processes, which will also be explored in future.

573

574 **Acknowledgements:** We thank NOAA's Climate Program Office for their support. We greatly

575 appreciate the helpful internal reviews by Drs. Hui Wang and Steve Baxter.

576 **References**

- 577 Arakawa, A., and W. H. Schubert, 1974: Interaction of a cumulus ensemble with the large-scale
578 environment, Part I. *J. Atmos. Sci.*, **31**, 674–704.
- 579 Bechtold, P., and co-authors, 2008: Advances in simulating atmospheric variability with the
580 ECMWF model: From synoptic to decadal time-scales. *Quart. J. Roy. Meteor. Soc.*, **134**,
581 1337–1351.
- 582 Crueger, T., B. Stevens, and R. Brokopf, 2013: The Madden-Julian oscillation in ECHAM6 and
583 the introduction of an objective MJO metric, *J. Clim.*, **26**, 3241–3257.
- 584 DeMott, C. A., N. P. Klingaman, and S. J. Woolnough, 2015: Atmosphere-ocean coupled
585 processes in the Madden-Julian oscillation, *Rev. Geophys.*, **53**, 1099–1154,
586 doi:10.1002/2014RG000478.
- 587 Flatau, M., P. J. Flatau, P. Phoebus, and P. P. Niler, 1997: The feedback between equatorial
588 convection and local radiative and evaporative processes: The implications for intraseasonal
589 oscillations, *J. Atmos. Sci.*, **54**, 2373–2386.
- 590 Fu, X., B. Yang, Q. Bao, and B. Wang, 2008: Sea surface temperature feedback extends the
591 predictability of tropical intraseasonal oscillation. *Mon. Wea. Rev.*, **136**, 577-597.
- 592 Grell, G. A., 1993: Prognostic evaluation of assumptions used by cumulus parameterization.
593 *Mon. Wea. Rev.*, **121**, 764–787.
- 594 Hendon, H. H., 2000: Impact of air-sea coupling on the Madden-Julian oscillation in a general
595 circulation model, *J. Atmos. Sci.*, **57**, 3939–3952.
- 596 Hung, M.-P., J.-L. Lin, W. Wang, D. Kim, T. Shinoda, and S. J. Weaver, 2013: MJO and
597 convectively coupled equatorial waves simulated by CMIP5 climate models. *J. Climate*, **26**,
598 6185–6124.

599 Inness, P. M., and J. M. Slingo, 2006: The interaction of the Madden-Julian oscillation with the
600 Maritime Continent in a GCM, *Q. J. R. Meteorol. Soc.*, **132**, 1645–1667.

601 Inness, P. M., and J. M. Slingo, 2003: Simulation of the Madden-Julian oscillation in a coupled
602 general circulation model. Part I: Comparison with observations and an atmosphere-only
603 GCM, *J. Clim.*, **16**, 345–364.

604 Inness, P. M., J. M. Slingo, E. Guilyardi, and J. Cole, 2003: Simulation of the Madden-Julian
605 oscillation in a coupled general circulation model. Part II: The role of the basic state, *J.*
606 *Clim.*, **17**, 365–382.

607 Jiang, X., and co-authors, 2015: Vertical structure and physical processes of the Madden-Julian
608 oscillation: Exploring key model physics in climate simulations, *J. Geophys. Res. Atmos.*,
609 **120**, 4718–4748, doi:10.1002/2014JD022374.

610 Joyce, R. J., J. E. Janowiak, P. A. Arkin, and P. Xie, 2004: CMORPH: A method that produces
611 global precipitation estimates from passive microwave and infrared data at high spatial and
612 temporal resolution. *J. Hydrometeor.*, **5**, 487–503.

613 Kemball-Cook, S., B. Wang, and X. Fu, 2002: Simulation of the intraseasonal oscillation in the
614 ECHAM-4 model: The impact of coupling with an ocean model. *J. Atmos. Sci.*, **59**, 1433–
615 1453.

616 Kim, D., J.-S. Kug, and A. H. Sobel, 2014: Propagating vs. Non-propagating Madden-Julian
617 oscillation events. *J. Climate*, **27**, 111–125.

618 Kim, H. M., D. Kim, F. Vitart, V. Toma, J. Kug, P. J. Webster, 2016: MJO propagation across
619 the Maritime Continent in the ECMWF ensemble prediction system, *J. Clim.*, 10.1175/JCLI-
620 D-15-0862.1.

621 Krishnamurti, T. N., D. K. Oosterhof, and A. V. Metha, 1988: Air-sea interaction on the
622 timescale of 30–50 days, *J. Atmos. Sci.*, **45**, 1304–1322.

623 Kumar, A., L. Zhang, and W. Wang, 2013: Sea surface temperature–precipitation relationship in
624 different reanalyses. *Mon. Wea. Rev.*, **141**, 1118–1123.

625 Liess, S., L. Bengtsson, and K. Arpe, 2004: The intraseasonal oscillation in ECHAM4. Part I:
626 Coupled to a comprehensive ocean model. *Clim. Dyn.*, **22**, 671–688.

627 Lin, J. L., and co-authors, 2006: Tropical intraseasonal variability in 14 IPCC AR4 climate
628 models. Part I: Convective signals, *J. Clim.*, **19**, 2665–2690.

629 Lin, J. L., M. I. Lee, D. Kim, I. S. Kang, and D. M. W. Frierson, 2008: Impact of convective
630 parameterization and moisture triggering on GCM simulated convectively coupled equatorial
631 waves. *J. Clim.*, **21**, 883–909.

632 Madden, R. A., and P. R. Julian, 1971: Detection of a 40–50 day oscillation in the zonal wind in
633 the tropical Pacific. *J. Atmos. Sci.*, **28**, 702–708.

634 Moorthi, S., and M. J. Suarez, 1992: Relaxed Arakawa–Schubert: A parameterization of moist
635 convection for general circulation models. *Mon. Wea. Rev.*, **120**, 978–1002.

636 Moorthi, S., and M. J. Suarez, 1999: Documentation of version 2 of relaxed Arakawa–Schubert
637 cumulus parameterization with convective downdrafts. NOAA Office Note 99-01, 44 pp.

638 Pan, H.-L., and W.-S. Wu, 1995: Implementing a mass flux convection parameterization package
639 for the NMC medium-range forecast model. NMC Office Note 409, 39 pp.

640 Pegion, K., and B. Kirtman, 2008: The impact of air–sea interactions on the predictability of the
641 tropical intraseasonal oscillation. *J. Climate*, **21**, 5870–5886.

642 Reynolds, R. W., T. M. Smith, C. Liu, D. B. Chelton, K. S. Casey, and M. G. Schlax, 2007:
643 Daily high-resolution blended analyses for sea surface temperature. *J. Climate*, **20**, 5473–
644 5496, doi:10.1175/2007JCLI1824.1.

645 Saha, S., and Coauthors, 2010: The NCEP Climate Forecast System Reanalysis. *Bull. Amer.*
646 *Meteor. Soc.*, **91**, 1015–1057, doi:10.1175/2010BAMS3001.1.

647 Saha, S., and Coauthors, 2014: The NCEP Climate Forecast System version 2. *J. Climate*, **27**,
648 2185–2208, doi:10.1175/JCLI-D-12-00823.1.

649 Seo, K.-H., W. Wang, J. Gottschalck, Q. Zhang, J.-K. E. Schemm, W. R. Higgins, and A.
650 Kumar, 2009: Evaluation of MJO forecast skill from several statistical and dynamical
651 forecast models. *J. Climate*, **22**, 2372–2388.

652 Seo, K.-H. and W. Wang, 2010: The Madden–Julian Oscillation Simulated in the NCEP Climate
653 forecast System Model: The Importance of Stratiform Heating. *J. Climate*, **23**, 4770–4793.

654 Shelly, A., P. Xavier, D. Copsey, T. Johns, J. M. Rodriguez, S. Milton, and N. Klingaman, 2014:
655 Coupled versus uncoupled hindcast simulations of the Madden–Julian Oscillation in the Year
656 of Tropical Convection. *Geophys. Res. Lett.*, **41**, 5670–5677.

657 Shinoda, T., H. H. Hendon, and J. Glick, 1998: Intraseasonal variability of surface fluxes and sea
658 surface temperature in the tropical western Pacific and Indian Oceans. *J. Climate*, **11**, 1685–
659 1702.

660 Slingo, J. M., and Coauthors, 1996: Intraseasonal oscillations in 15 atmospheric general
661 circulation models: Results from an AMIP diagnostic subproject. *Clim. Dyn.*, **12**, 325–357.

662 Tokioka, T., K. Yamazaki, A. Kitoh, and T. Ose, 1988: The equatorial 30–60 day oscillation and
663 the Arakawa–Schubert penetrative cumulus parameterization. *J. Meteor. Soc. Japan*, **66**,
664 883–901.

665 Vitart, F., and Coauthors, 2007: Monthly forecast of the Madden–Julian oscillation using a
666 coupled GCM. *Mon. Wea. Rev.*, **135**, 2700–2715.

667 Waliser, D. E., K. M. Lau, and J.-H. Kim, 1999: The influence of coupled SSTs on the Madden–
668 Julian oscillation: A model perturbation experiment. *J. Atmos. Sci.*, **56**, 333–358.

669 Wang, W., M.-P. Hung, S. J. Weaver, A. Kumar, and X. Fu, 2014: MJO prediction in the NCEP
670 Climate Forecast System version 2. *Clim. Dyn.*, **42**, 2509–2520.

671 Wang, W., A. Kumar, J. X. Fu, and M.-P. Hung, 2015: What is the Role of the Sea Surface
672 Temperature Uncertainty in the Prediction of Tropical Convection Associated with the
673 MJO?. *Mon. Wea. Rev.*, **143**, 3156–3175.

674 Wang, W., and M. Schlesinger, 1999: The dependence on convection parameterization of the
675 tropical intraseasonal oscillation simulated by the UIUC 11-layer atmospheric GCM. *J.*
676 *Climate*, **12**, 1423–1457.

677 Weaver, S. J., W. Wang, M. Chen, and A. Kumar, 2011: Representation of the MJO variability
678 in the NCEP Climate Forecast System. *J. Climate*, **24**, 4676–4694.

679 Woolnough, S. J., J. M. Slingo, and B. J. Hoskins, 2000: The relationship between convection
680 and sea surface temperature on intraseasonal timescales. *J. Climate*, **13**, 2086–2104.

681 Zhang, C., 2005: Madden-Julian Oscillation. *Rev. of Geophys.*, **43**, RG2003,
682 doi:10.1029/2004RG000158.

683 Zhang, C., M. Dong, S. Gualdi, H. H. Hendon, E. D. Maloney, A. Marshall, K. R. Sperber, and
684 W. Wang, 2006: Simulations of the Madden-Julian oscillation in four pairs of coupled and
685 uncoupled global models, *Clim. Dyn.*, **27**, 573–592.

686 Zhang, G. J., and M. Mu, 2005: Simulation of the Madden–Julian Oscillation in the NCAR
687 CCM3 using a revised Zhang–McFarlane convection parameterization scheme. *J. Climate*,
688 **18**, 4046–4064.

689 **Tables:**

690 Table 1. Description of experiments

Experiments	Model	Convection Schemes	SST nudging (restoring time scale)
CFSv2_RAS	CFSv2	RAS	No
CFSv2L_RAS	CFSv2L	RAS	No
CFSv2L_RAS_SST1dy	CFSv2L	RAS	Yes (1 day)
CFSv2L_RAS_SST10dy	CFSv2L	RAS	Yes (10 days)
CFSv2_SAS	CFSv2	SAS	No

691

692 **Figures Captions:**

693 **Figure 1.** November-April lag-longitude diagram of 10°S–10°N averaged intraseasonal (20–100-
694 day filtered) precipitation anomalies (colors) and 850-hPa zonal wind anomalies [contours;
695 (m/s)/(mm/day)] regressed against the Indian Ocean precipitation (70-100°E, 10°S-10°N) for
696 (a) CFSv2_RAS, (b) CFSv2_SAS, (c) observation (CMORPH precipitation and CFSR wind),
697 (d) CFSv2L_RAS, (e) CFSv2L_RAS_SST10dy and (f) CFSv2L_RAS_SST1dy. Contour
698 interval is 0.1 (m/s)/(mm/day) with the zero contour omitted.

699 **Figure 2.** As in Fig. 1, except with contours for SST anomalies. SST is plotted at -0.09, -0.06, -
700 0.03, -0.02, -0.01, 0.01, 0.02, 0.03, 0.06 and 0.09 °C/(mm/day).

701 **Figure 3.** As in Fig. 1, except with colors for SST anomalies [$0.1^{\circ}\text{C}/(\text{mm}/\text{day})$] and contours
702 for surface net downward shortwave flux anomalies [SWF; $(\text{W}/\text{m}^2)/(\text{mm}/\text{day})$]. SWF is
703 plotted at -9, -6, -3, -2, -1, -0.5, 0.5, 1, 2, 3, 6 and 9 $(\text{W}/\text{m}^2)/(\text{mm}/\text{day})$.

704 **Figure 4.** As in Fig. 3, except with contours for surface downward latent heat flux anomalies
705 [LHF; $(\text{N}/\text{m}^2)/(\text{mm}/\text{day})$]. LHF is plotted at -9, -6, -3, -2, -1, -0.5, 0.5, 1, 2, 3, 6 and 9
706 $(\text{W}/\text{m}^2)/(\text{mm}/\text{day})$.

707 **Figure 5.** November-April correlations between the intraseasonal (20–100-day filtered)
708 precipitation anomalies over the Indian Ocean (70-100°E, 10°S-10°N) and the intraseasonal
709 LHF anomalies over (120-140°E, 10°S-10°N) for observation (CMORPH precipitation and
710 CFSR heat flux; blue curves), CFSv2_RAS (red curves), and CFSv2_SAS (green curves).

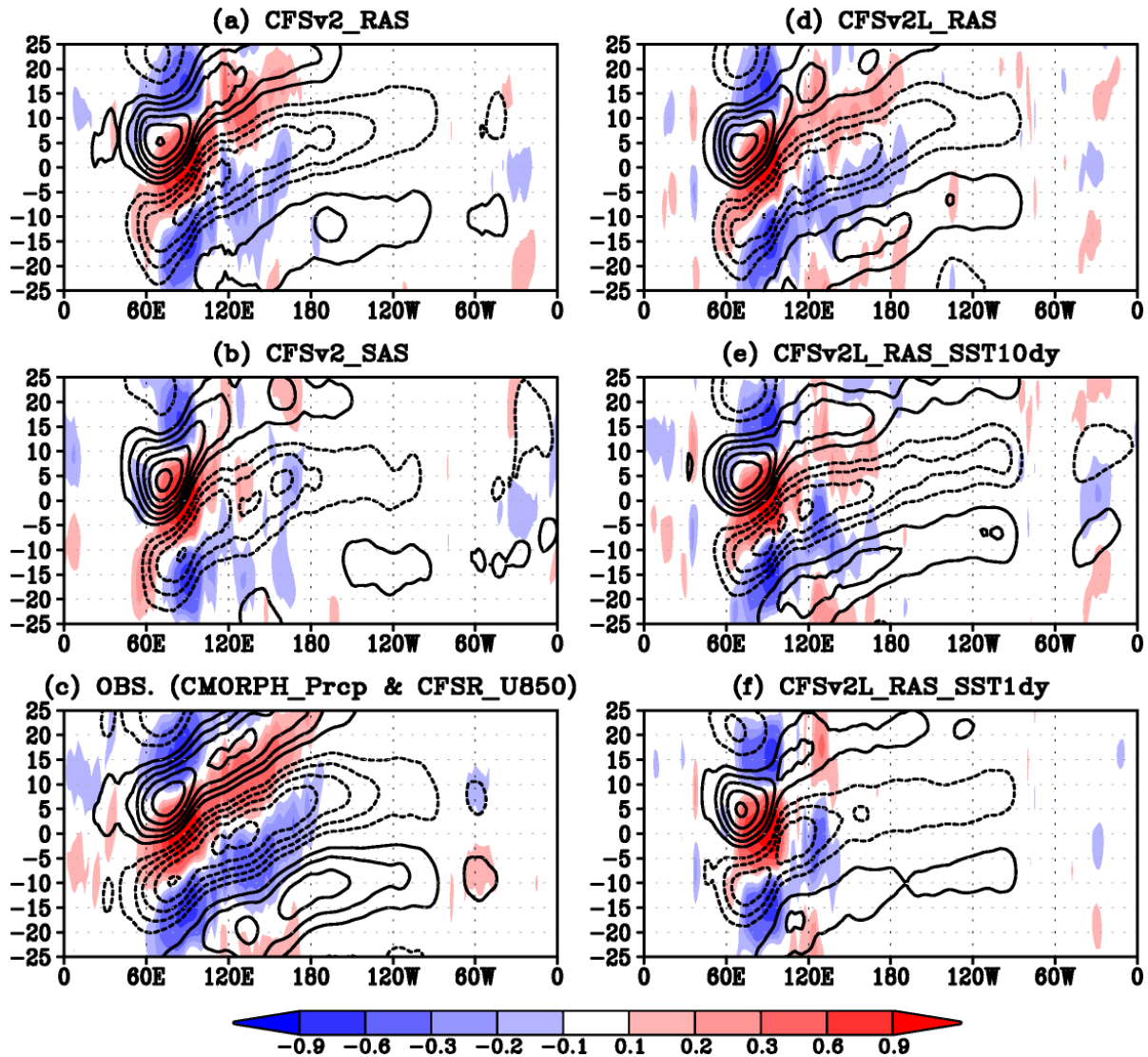
711 **Figure 6.** November-April lead-lag regressions of different terms affecting the intraseasonal
712 LHF anomalies [averaged over (120-140°E, 10°S-10°N)] against the Indian Ocean
713 precipitation (70-100°E, 10°S-10°N) for (a) observation (CFSR), (b) CFSv2_RAS, and (c)
714 CFSv2_SAS. The solid black curves are for δE (corresponding to curves in Fig. 5), with the

715 red, green, blue curves for $\delta w(\bar{q}_a - \bar{q}_s)$, $\bar{w}\delta q_a$ and $-\bar{w}\delta q_s$, respectively. The dashed curves
716 are for the residual term. Unit is (m/s)/(mm/day).

717 **Figure 7.** November-April lead-lag regressions of the intraseasonal w^2 , u^2 and v^2 anomalies
718 [averaged over (120-140°E, 10°S-10°N)] against the Indian Ocean precipitation (70-100°E,
719 10°S-10°N) for (a) observation (CFSR), (b) CFSv2_RAS, and (c) CFSv2_SAS. The red
720 curves are for $-w^2$ (corresponding to red curves in Fig. 6), and the blue (green) curves are for -
721 u^2 ($-v^2$). Unit is (m/s)²/(mm/day). Note that regressions are calculated for the opposite of w^2 ,
722 u^2 and v^2 , which is to coincide with the sign of surface heat flux into the ocean.

723 **Figure 8.** November-April regressions of the intraseasonal w^2 , u^2 and v^2 anomalies against the
724 Indian Ocean precipitation (70-100°E, 10°S-10°N) for (a) observation (CFSR), (b)
725 CFSv2_RAS, and (c) CFSv2_SAS. The regressions are shown as averages over 10 ~ 1 days
726 when precipitation lags the formers. The left (right) column is for $-w^2$ and $-u^2$ ($-v^2$), with the
727 former colored and the latter contoured. Unit is (m/s)²/(mm/day).

Regression of 10S–10N PRCP(shaded)/U850(contour) onto IO PRCP



728

729

730

731

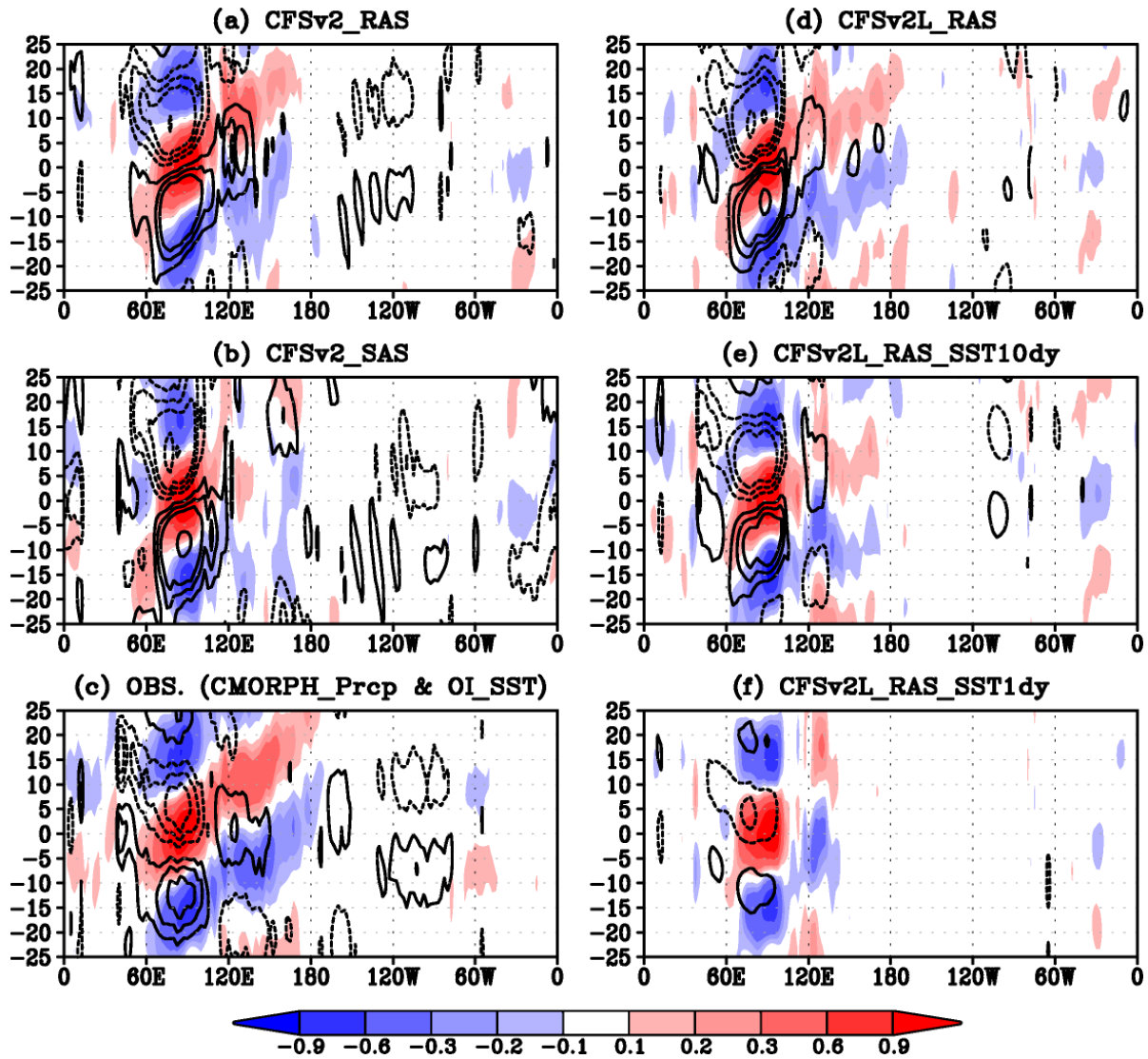
732

733

734

Figure 1. November–April lag–longitude diagram of 10°S–10°N averaged intraseasonal (20–100-day filtered) precipitation anomalies (colors) and 850-hPa zonal wind anomalies [contours; (m/s)/(mm/day)] regressed against the Indian Ocean precipitation (70–100°E, 10°S–10°N) for (a) CFSv2_RAS, (b) CFSv2_SAS, (c) observation (CMORPH precipitation and CFSR wind), (d) CFSv2L_RAS, (e) CFSv2L_RAS_SST10dy and (f) CFSv2L_RAS_SST1dy. Contour interval is 0.1 (m/s)/(mm/day) with the zero contour omitted.

Regression of 10S–10N PRCP(shaded)/SST(contour) onto IO PRCP



735

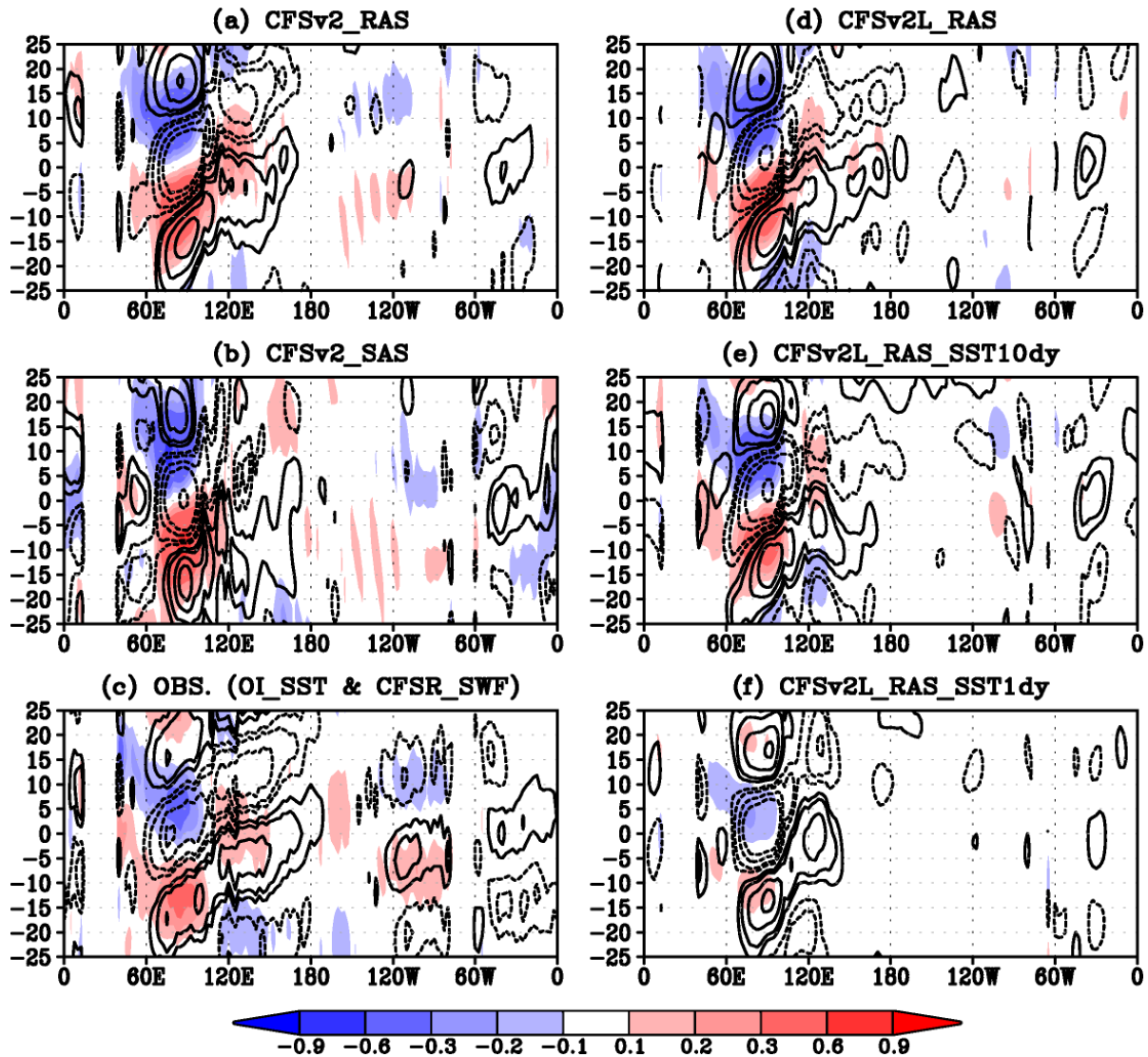
736

Figure 2. As in Fig. 1, except with contours for SST anomalies. SST is plotted at -0.09, -0.06, -

737

0.03, -0.02, -0.01, 0.01, 0.02, 0.03, 0.06 and 0.09 °C/(mm/day).

Regression of 10S–10N SST(shaded)/SWF(contour) onto IO PRCP



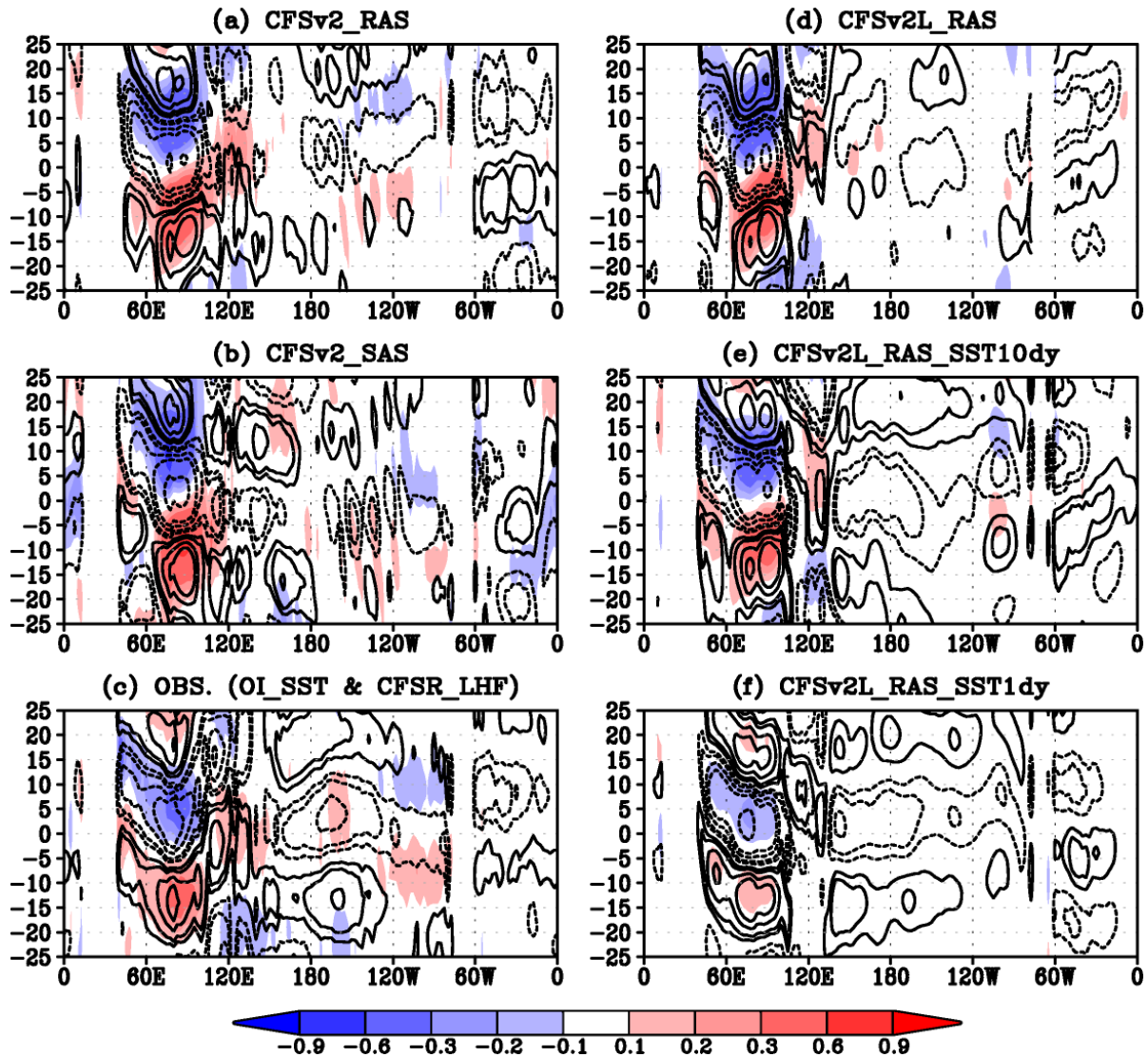
738

739 **Figure 3.** As in Fig. 1, except with colors for SST anomalies [$0.1^{\circ}\text{C}/(\text{mm}/\text{day})$] and contours

740 for surface net downward shortwave flux anomalies [SWF; $(\text{W}/\text{m}^2)/(\text{mm}/\text{day})$]. SWF is

741 plotted at -9, -6, -3, -2, -1, -0.5, 0.5, 1, 2, 3, 6 and 9 $(\text{W}/\text{m}^2)/(\text{mm}/\text{day})$.

Regression of 10S–10N SST(shaded)/LHF(contour) onto IO PRCP



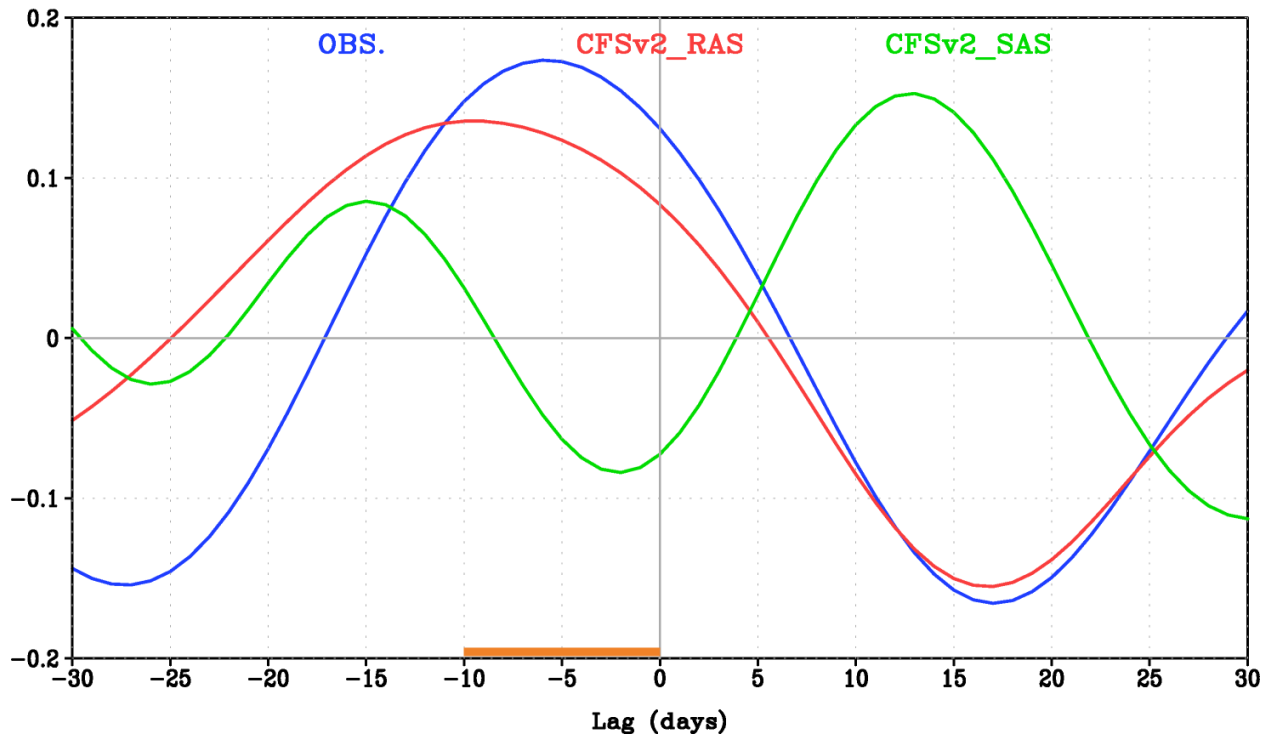
742

743 **Figure 4.** As in Fig. 3, except with contours for surface downward latent heat flux anomalies

744 [LHF; (N/m²)/(mm/day)]. LHF is plotted at -9, -6, -3, -2, -1, -0.5, 0.5, 1, 2, 3, 6 and 9

745 (W/m²)/(mm/day).

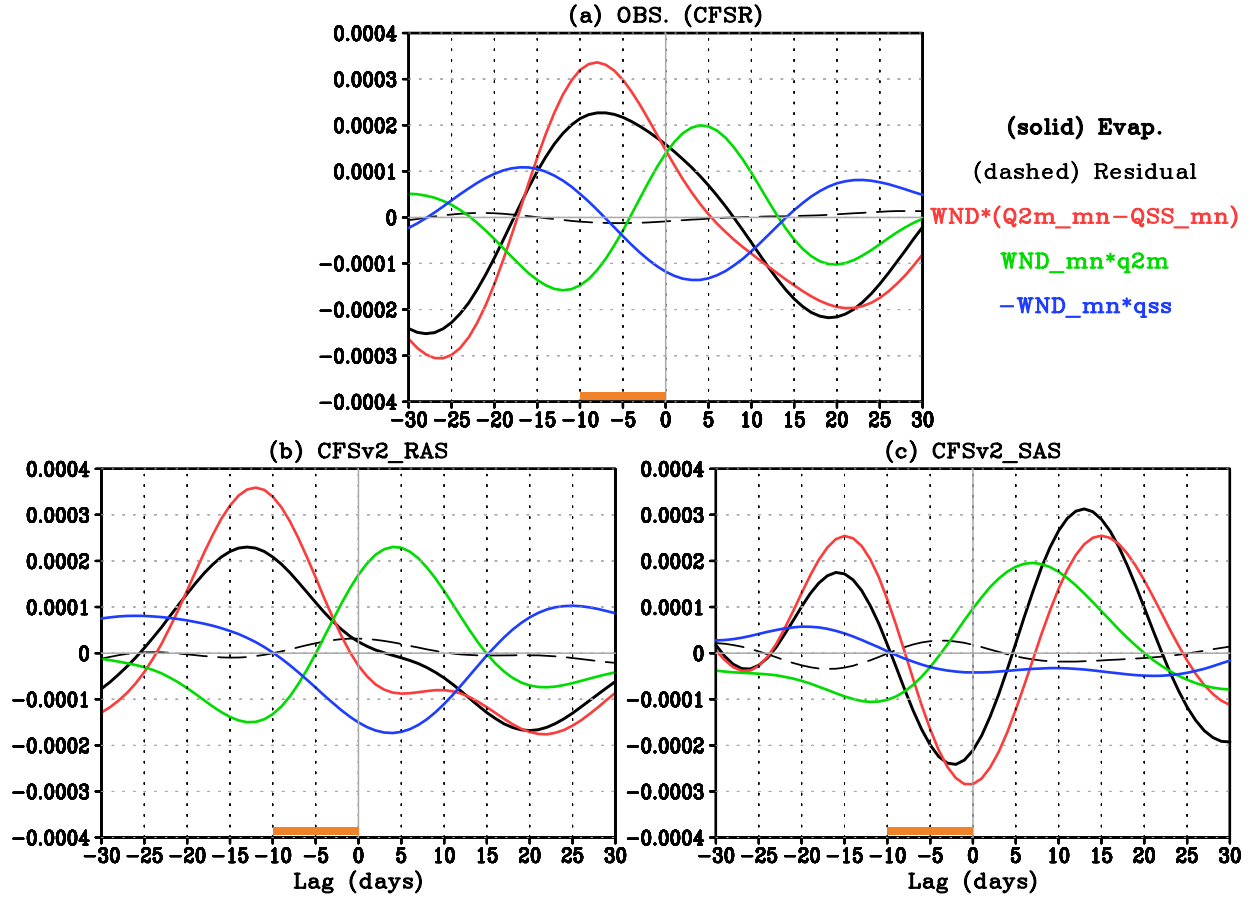
Corr. between IO PRCP and LHF in (120–140E,10S–10N)



746

747 **Figure 5.** November-April correlations between the intraseasonal (20–100-day filtered)
748 precipitation anomalies over the Indian Ocean (70-100°E, 10°S-10°N) and the intraseasonal
749 LHF anomalies over (120-140°E, 10°S-10°N) for observation (CMORPH precipitation and
750 CFSR heat flux; blue curves), CFSv2_RAS (red curves), and CFSv2_SAS (green curves).

Regression of Evap. terms over (120–140E,10S–10N) onto IO PRCP



751

752 **Figure 6.** November-April lead-lag regressions of different terms affecting the intraseasonal

753 LHF anomalies [averaged over (120-140°E, 10°S-10°N)] against the Indian Ocean

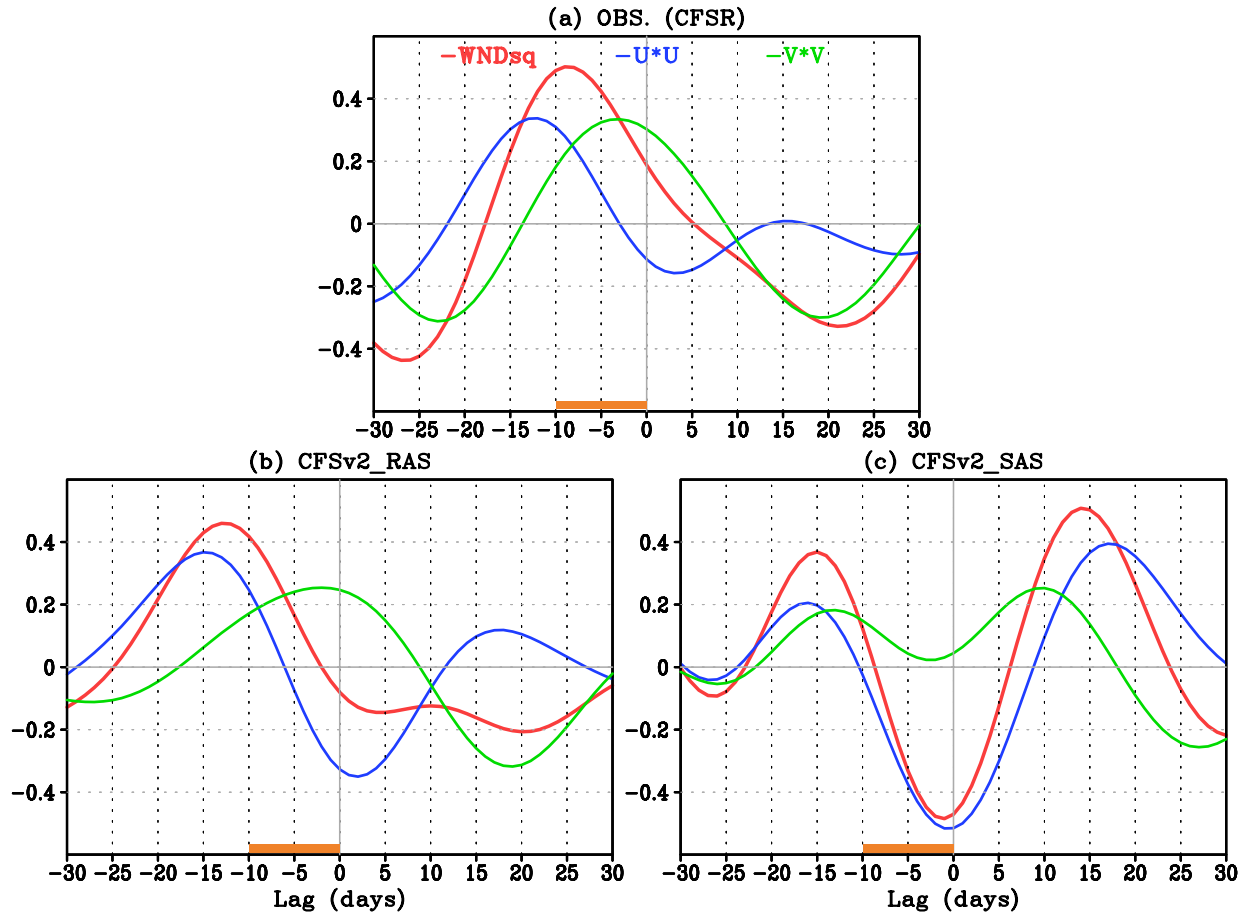
754 precipitation (70-100°E, 10°S-10°N) for (a) observation (CFSR), (b) CFSv2_RAS, and (c)

755 CFSv2_SAS. The solid black curves are for δE (corresponding to curves in Fig. 5), with the

756 red, green, blue curves for $\delta w(\bar{q}_a - \bar{q}_s)$, $\bar{w}\delta q_a$ and $-\bar{w}\delta q_s$, respectively. The dashed curves

757 are for the residual term. Unit is (m/s)/(mm/day).

Regression of WNDsq terms over (120–140E,10S–10N) onto IO PRCP



758

759 **Figure 7.** November-April lead-lag regressions of the intraseasonal w^2 , u^2 and v^2 anomalies

760 [averaged over (120-140°E, 10°S-10°N)] against the Indian Ocean precipitation (70-100°E,

761 10°S-10°N) for (a) observation (CFSR), (b) CFSv2_RAS, and (c) CFSv2_SAS. The red

762 curves are for $-w^2$ (corresponding to red curves in Fig. 6), and the blue (green) curves are for $-$

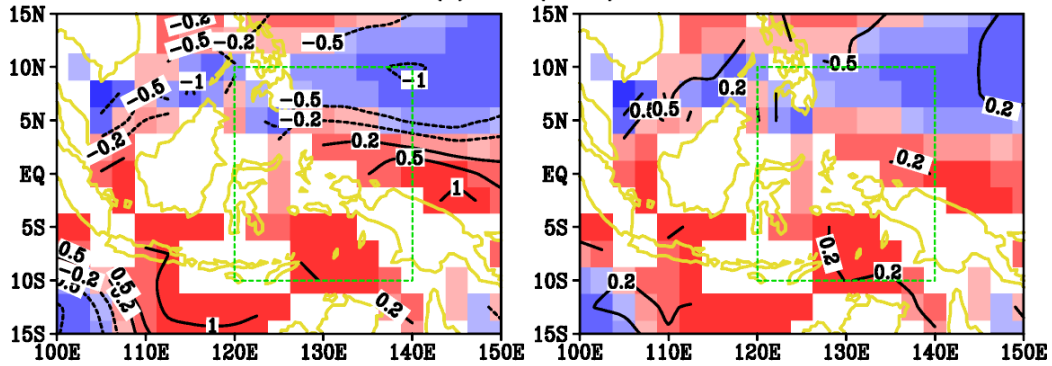
763 u^2 ($-v^2$). Unit is $(\text{m/s})^2/(\text{mm/day})$. Note that regressions are calculated for the opposite of w^2 ,

764 u^2 and v^2 , which is to coincide with the sign of surface heat flux into the ocean.

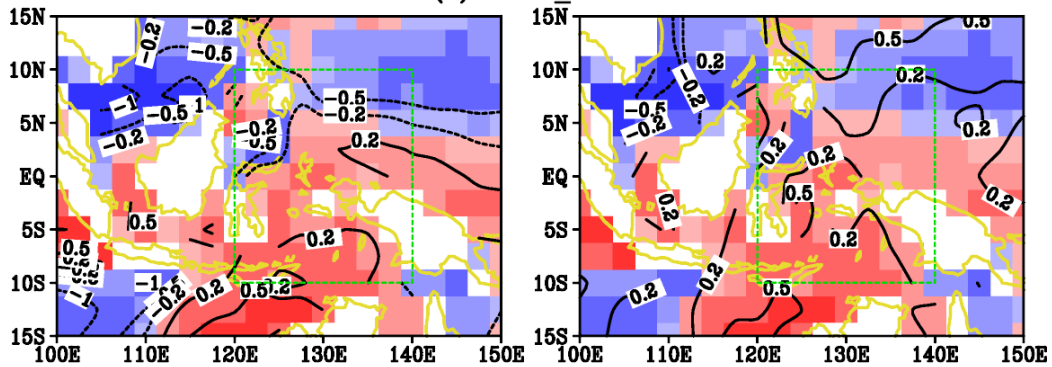
Regression of WNDsq terms over onto IO PRCP (ld=-10~-1days)

-WNDsq(shading) & -U*U(contour) -WNDsq(shading) & -V*V(contour)

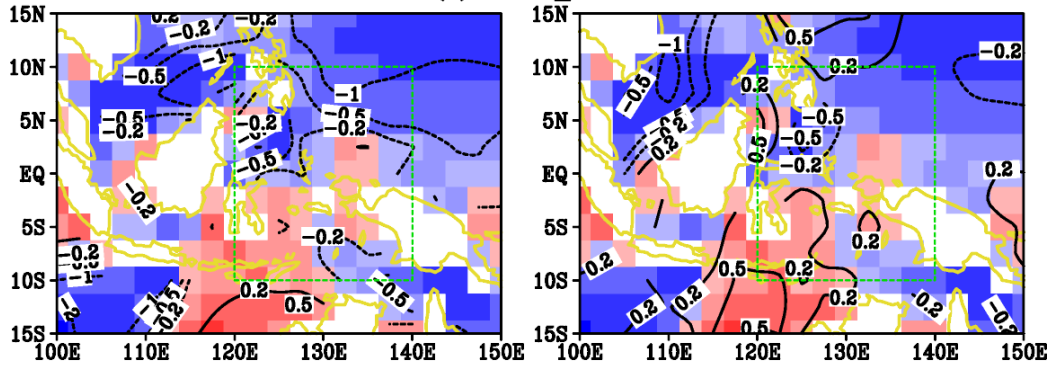
(a) OBS.(CFSR)



(b) CFSv2_RAS



(c) CFSv2_SAS



765

766

767

768

769

770

Figure 8. November-April regressions of the intraseasonal w^2 , u^2 and v^2 anomalies against the Indian Ocean precipitation (70-100°E, 10°S-10°N) for (a) observation (CFSR), (b) CFSv2_RAS, and (c) CFSv2_SAS. The regressions are shown as averages over 10 ~ 1 days when precipitation lags the formers. The left (right) column is for $-w^2$ and $-u^2$ ($-v^2$), with the former colored and the latter contoured. Unit is $(\text{m/s})^2/(\text{mm/day})$.